Dissociation dynamics of noble-gas dimers in intense two-color IR laser fields

M. Magrakvelidze and U. Thumm

J. R. Macdonald Laboratory, Department of Physics, Kansas State University, Manhattan, Kansas 66506, USA

(Received 8 May 2013; published 16 July 2013)

We numerically model the dissociation dynamics of the noble-gas dimer ions He_2^+, Ne_2^+, Ar_2^+, Kr_2^+, and Xe_2^+ in ultrashort pump and probe laser pulses of different wavelengths. Our calculations reveal a distinguished "gap" in the kinetic energy spectra, observed experimentally for the Ar_2 dimer [J. Wu *et al.*, Phys. Rev. Lett. **110**, 033005 (2013)], for all noble-gas dimers for appropriate wavelength combinations. This striking phenomenon can be explained by the dissociation of dimer ions on dipole-coupled Born-Oppenheimer adiabatic potential curves. Comparing pump-probe-pulse-delay-dependent kinetic-energy-release spectra for different noble-gas dimer cations of increasing mass, we discuss increasingly prominent (i) fine-structure effects in and (ii) classical aspects of the nuclear vibrational motion.

DOI: 10.1103/PhysRevA.88.013413 PACS number(s): 33.80.Rv, 34.50.Gb

I. INTRODUCTION

Advances in laser technology made it possible to control and image the nuclear wave-packet dynamics of diatomic molecules in real time [1,2]. In particular, pump-probe-spectroscopic imaging is being employed to trace the nuclear motion in both the smallest diatomic molecules, H_2 and D_2 [3–6], and heavier diatomic molecules, such as O_2, N_2, and CO [7–9], most recently including XUV-pump-XUV-probe experiments at free-electron laser facilities [10,11]. In these experiments the pump pulse primarily ionizes the neutral molecule while a delayed probe pulse dissociates the molecular ion, revealing the nuclear dynamics in the bound and dissociating molecular ions through pump-probe-delay-dependent kinetic-energy-release (KER) spectra.

Noble-gas dimers are more weakly bound and have much larger vibrational periods than the diatomic molecules mentioned above. Dissociation energies of neutral noble-gas dimers (X_2) are in the 1–25 meV range, orders of magnitude below the dissociation energy of the corresponding dimer cations X_2^+ (Table I). The vibrational periods of the dimer cations in their electronic ground states are of the order of hundreds of femtoseconds, an order of magnitude larger than those of H_2^+, O_2^+, N_2^+, and CO^+ (Table II). Another characteristic feature of all noble-gas dimers is that the equilibrium distance of the neutral dimer is larger than for the dimer ion. Dimer ions therefore contract upon photoionization of the neutral parent molecule, before the molecular-ion nuclear wave packet reflects at the inner turning point of its adiabatic molecular state (Figs. 1–3). These features, especially the comparatively slow nuclear motion, make noble-gas dimers and their cations very attractive targets for the detailed investigation of their bound and dissociative nuclear dynamics in pump-probe experiments. Such investigations are of relevance for modeling of the larger clusters [12]. Neutral noble-gas dimers are metastable but can be used in pump-probe experiments if cooled [13].

In this work we study the dissociative ionization of noble-gas dimers X_2 (X = He, Ne, Ar, Kr, and Xe) by numerical simulation and analysis of KER spectra as a function of the pump-probe-pulse delay. Of particular interest to this study is to find out whether the "delay gap" in measured and calculated KER spectra for Ar_2 dimer cations [14] can also be observed in other noble-gas dimers and explained within the same two-color "pump-dump" mechanism. This paper is organized as follows. Section II explains our numerical model. Numerical results are presented and analyzed in Sec. III. In particular, in Sec. III A we discuss results for the nuclear dynamics on a single adiabatic potential curve of each dimer cation. Classical and quantum aspects of the dissociation process are examined in Sec. III B. KER spectra resulting from calculations that include dipole-coupled adiabatic molecular curves of the cations, with and without including electronic fine structure, are shown and discussed in Sec. III C, followed by a brief summary in Sec. IV. Throughout this work we use atomic units unless indicated otherwise.

II. MODEL

Using a pump-probe sequence of intense laser pulses, the nuclear motion in X_2^+ can be traced in KER spectra as a function of the delay between the two pulses. Figure 1 shows the pump-probe process schematically, where the pump pulse singly ionizes an X_2 dimer. The delayed probe pulse has a different wavelength than the pump pulse and dissociates the ionized dimer ($X_2^+ \rightarrow X + X^+$). Several dissociation paths are possible, depending on the central wavelength of the laser pulses. After ionization of the neutral dimer, the cation nuclear wave packet starts moving inward from point A on the lowest X_2^+ adiabatic potential curve V_1 [corresponding to either the X_2^+ electronic state $^2\Sigma_u^+$ without including or $I(1/2)_u$ including spin-orbit (SO) couplings (fine structure)] to the one-photon crossing points B (ω_1) and C (ω_2), where it may undergo a laser-induced transition to an excited adiabatic electronic state with potential curve V_2 of X_2^+ [$^2\Sigma_g^+$ or $II(1/2)_g$]. The cation subsequently dissociates along the excited-state potential curve, leading to two distinct energy bands in the KER spectra for the paths *ABE* and *ACD*.

We perform two kinds of calculations. We first conduct single-cation-curve calculations, in order to identify and characterize the oscillatory motion of the nuclear wave packet in either the $^2\Sigma_u^+$ or $I(1/2)_u$ bound adiabatic electronic state of X_2^+. Calculating the nuclear wave-packet probability density as a function of propagation time and internuclear distance R, we obtain wave-packet revival times [15] and oscillation periods in a given adiabatic molecular state [8]. Our Crank-Nicholson split-operator nuclear wave-packet

TABLE I. Selected properties of noble-gas dimers (X_2) and their cations (X_2^+). Column 2, reduced mass; 3, equilibrium distance $R_0(X_2)$ of the ground state of neutral dimer; 4, equilibrium distance of the dimer cation $R_0(X_2^+)$ without SO coupling; 5, dissociation energy of the neutral dimer ground state $D_e(X_2)$, 6, dimer cation dissociation energy in the ground state $D_e(X_2^+)$ without spin-orbit coupling; 7, dissociation energy in the ground state $D_e(X_2^+)$ with spin-orbit coupling; 8, ionization energy I_p of X_2; 9, spin-orbit splitting of X_2^+ (eV); and 10, full width at half maximum of the ground-state dimer nuclear probability density.

1	2	3	4	5	6	7	8	9	10
Dimer	Reduced mass of X_2 (a.u.)	$R_0(X_2)$ (a.u.)	$R_0(X_2^+)$ (a.u.)	D_e (X_2) (meV)	D_e (X_2^+) $^2\Sigma_u^+$(eV)	$D_e(X_2^+)$ $I(1/2)_u$ (eV) [28]	I_p (eV) of X_2 [29]	SO splitting of X_2^+ (eV)	Width of X_2 vibrational ground state (a.u.)
He_2	3651.91	5.61 [18]	2.4 [19]	0.94 [18]	2.5 [19]		24.6		15
Ne_2	18411.65	5.8 [20]	3.3 [23]	3.6 [20]	1.2 [21]	1.17	21.76	0.096 [23]	1.6
Ar_2	36447.90	7.1 [22]	4.6 [22,23]	12.3 [22]	1.24 [28]	1.19	14.51	0.18 [22,23]	1.0
Kr_2	76456.01	7.6 [25]	5.0 [23]	17.3 [25]	1.23 [28]	1.05	12.87	0.67 [23]	0.7
Xe_2	119789.70	8.3 [25]	5.9 [27]	24.4 [25]	1.08 [28]	0.79	11.24	1.31 [27]	0.3

propagation calculations [8,16] were done with time steps $\Delta t = 1$, equidistant spacings $\Delta R = 0.01$ of the internuclear-distance grid, and a numerical-grid length of $R_{\max} = 100$ (excluding the absorber length). In order to prevent unphysical reflections at the end of the numerical grid, we included an absorber [16] that covers a grid length of 10 a.u. In a second, improved set of calculations we allow for dipole coupling of cation states in the electronic fields of the pump and probe laser. These calculations were done with a numerical-grid length of $R_{\max} = 330$ (excluding an absorber with a length of 20 a.u.), and the same grid spacing and time steps as for the single-cation-curve calculation. All KERs were calculated for a pump-probe delay range between 0 and 800 fs.

The adiabatic molecular potential energy curves used in our calculations are shown in Fig. 2 without including SO couplings and in Fig. 3 including SO couplings [17–29]. The dipole coupling matrix elements between the $I(1/2)_u$ and $II(1/2)_g$ ($^2\Sigma_u^+$ and $^2\Sigma_g^+$) X_2^+ states for calculations that include (do not include) SO couplings, were taken from Refs. [19,24,27,28]. He_2 is the weakest bound noble-gas dimer with a dissociation energy of ∼1 meV. It is the only noble-gas dimer for which the two lowest cation states are not SO split. The SO splitting for the low-lying states of He_2^+ is absent because it only has σ electrons [30].

A. Single-cation-curve calculation

In this section we allow the cation nuclear vibrational wave packet to freely propagate on the lowest adiabatic potential curves $V_1(R)$ of the dimer cation X_2^+ and compare results obtained without including SO coupling ($V_1 = {}^2\Sigma_u^+$) and including SO coupling [$V_1 = I(1/2)_u$]. The maximal propagation times in our numerical applications in Sec. III below are significantly smaller than the rotational periods of the dimer cations (2.3 ps for He_2^+ [29], 30 ps for Ne_2^+ [29], 122 ps for Ar_2^+ [28], 320 ps for Kr_2^+ [28], and 694 ps for Xe_2^+ [28]). We can, therefore, neglect the rotation of the dimer and solve the time-dependent Schrödinger equation (TDSE) for the vibrational nuclear motion,

$$i\frac{d}{dt}\Psi_1 = [T_R + V_1(R)]\Psi_1, \tag{1}$$

where $T_R = -(1/M)\,\partial^2/\partial R^2$ is the kinetic energy operator for the relative motion of the two nuclei with individual mass M.

Starting with the neutral dimer (X_2) in the ground state, we first modeled the creation of the initial X_2^+ vibrational wave packet by the pump pulse in Frank-Condon (FC) approximation [30–32]. In an attempt to more "realistically" describe the ionization process, we performed comparative calculations modeling the ionization in the pump pulse based on molecular Ammosov-Delone-Krainov (ADK) ionization rates $\Gamma_{\rm ADK}$ [16,33]. We obtained almost identical numerical results for modeling the ionization step in FC approximation and with ADK rates, very small quantitative differences being irrelevant for the discussion and conclusion reached in this work. All numerical results shown in this paper are derived

TABLE II. Number of vibrational bound states, revival times, and wave-packet-oscillation periods for nuclear vibrational wave packets in the $I(1/2)_u$ and $^2\Sigma_u^+$ adiabatic electronic states of X_2^+ dimers. The variance $(\Delta R)^2$ in the last column is calculated at one vibrational oscillation period past the center of the pump pulse. Our calculations do not allow the determination of a vibrational oscillation period for He_2^+. Due to the absence of fine-structure effects in He_2^+, no results are quoted for the $I(1/2)_u$ state.

	$^2\Sigma_u^+$			$I(1/2)_u$			
Dimer	Number of bound vibrational states	Oscillation period (fs)	Revival times (ps)	Number of bound vibrational states	Oscillation period (fs)	Revival times (ps)	Variance $(\Delta R)^2$ (a.u.) calculated at $\tau + T_{\rm osc}$
He_2^+	23		∼0.5				>12
Ne_2^+	41	250	2.8	32	230	2.2	0.85
Ar_2^+	69	290	7.9	63	250	7.5	0.15
Kr_2^+	111	490	22	91	460	19.0	0.09
Xe_2^+	149	550	39	131	510	38.2	0.03

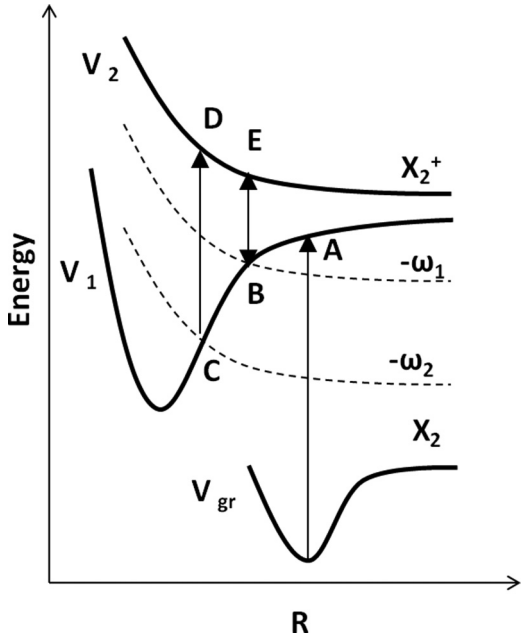

FIG. 1. Schematics of the nuclear wave-packet motion on generic X_2 and X_2^+ adiabatic molecular potential curves. Point A indicates the center of the Franck-Condon region, points B–E and C–D correspond to one-photon transitions mediated by laser pulses of frequencies ω_1 (1400 or 700 nm) and ω_2 (800 or 500 nm). V_{gr} designates the ground-state adiabatic potential curve of X_2. V_1 and V_2 are the two lowest adiabatic potential curves of X_2^+.

with ADK rates. We solve (1) numerically for the initial vibrational wave packet in the dimer cation

$$\Psi_1(R,t=0)=\sum_v a_{1,v}\varphi_{1,v}(R) \tag{2}$$

that can be viewed as coherent superposition of vibrational states $\varphi_{1,v}$ in the adiabatic potential $V_1(R)$ with amplitudes $a_{1,v}=\langle\varphi_{1,v}|\Psi_{gr}(R,t=0)\rangle$, where $\Psi_{gr}(R,t=0)$ is the ground state of the neutral dimer. Time propagation of (1) subject to the initial condition (2) results in the (laser-electric) field-free time-dependent nuclear vibrational wave function

$$\Psi_1(R,t)=\sum_v a_{1,v}\varphi_{1,v}(R)e^{-i\omega_{1,v}t}, \tag{3}$$

where $\omega_{1,v}$ is the vibrational energy in state $\varphi_{1,v}$. Examining the nuclear probability density

$$\rho_1(R,t)=|\Psi_1(R,t)|^2 \tag{4}$$

as a function of the propagation time t in $V_1(R)$ allows us to identify oscillation periods and revival times [9,15].

B. Dipole-coupled calculations

Ionization of the neutral dimer by the pump and probe pulses launches vibrational wave packets Ψ_1 and Ψ_2 in both the lowest bonding state [$^2\Sigma_u^+$ or $I(1/2)_u$] of the dimer cation on the adiabatic potential curve V_1 and the first excited repulsive state [$^2\Sigma_g^+$ or $II(1/2)_g$] on V_2, respectively. The initial population of the X_2^+ excited state by ionization of X_2 leads to immediate dissociation and merely accounts for a delay-independent increase of the KER yield at KERs between 1 and 2 eV in the KER spectra discussed below. The subsequent motion of this initial nuclear wave packet $\Psi_2(R)$ on the repulsive curve $V_2(R)$ is thus of minor relevance for our investigation. In our numerical simulations we therefore assume that the ionization step exclusively populates the binding X_2^+ states on V_1 and allows for coupling of the nuclear motion to V_2 exclusively by laser-induced dipole transitions between the adiabatic electronic states associated

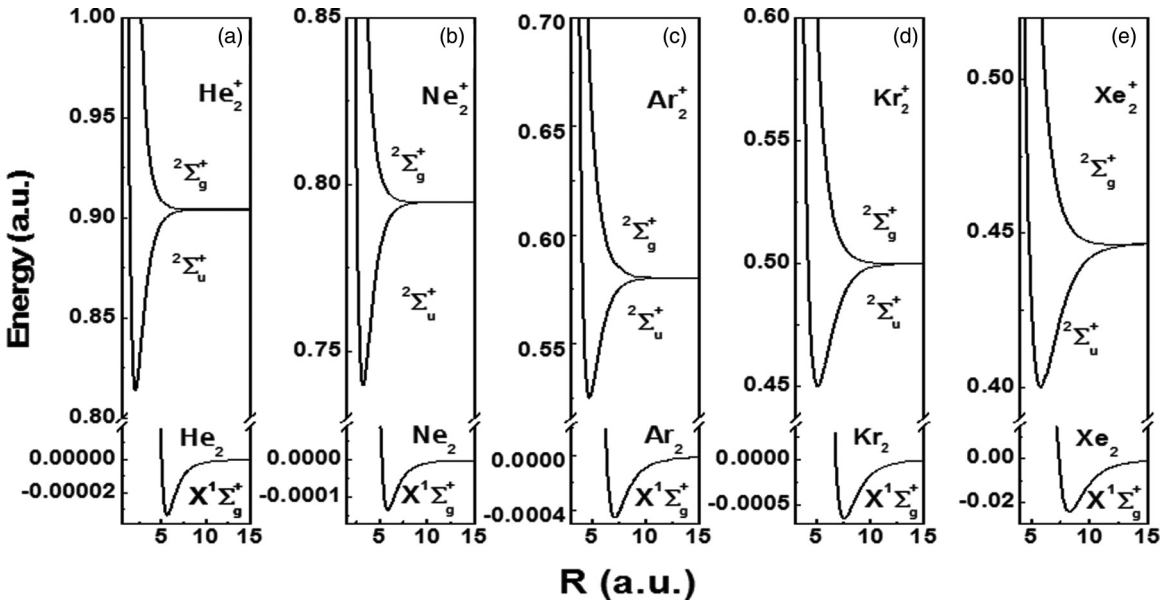

FIG. 2. Adiabatic potential energy curves for X_2 and X_2^+ dimers, calculated without including spin-orbit coupling. (a) Ground state of He_2 (adapted from [17,18]) and the two lowest states of He_2^+ (from [19]). (b) Ground state of Ne_2 (from [20]) and the two lowest states of Ne_2^+ (from [21,23]). (c) Ground state of Ar_2 (from [22]) and the two lowest states of Ar_2^+ (from [22–24]). (d) Ground state of Kr_2 (from [25]) and the two lowest states of Kr_2^+ (from [26]). (e) Ground state of Xe_2 (from [25]) and the two lowest states of Xe_2^+ (from [27]).

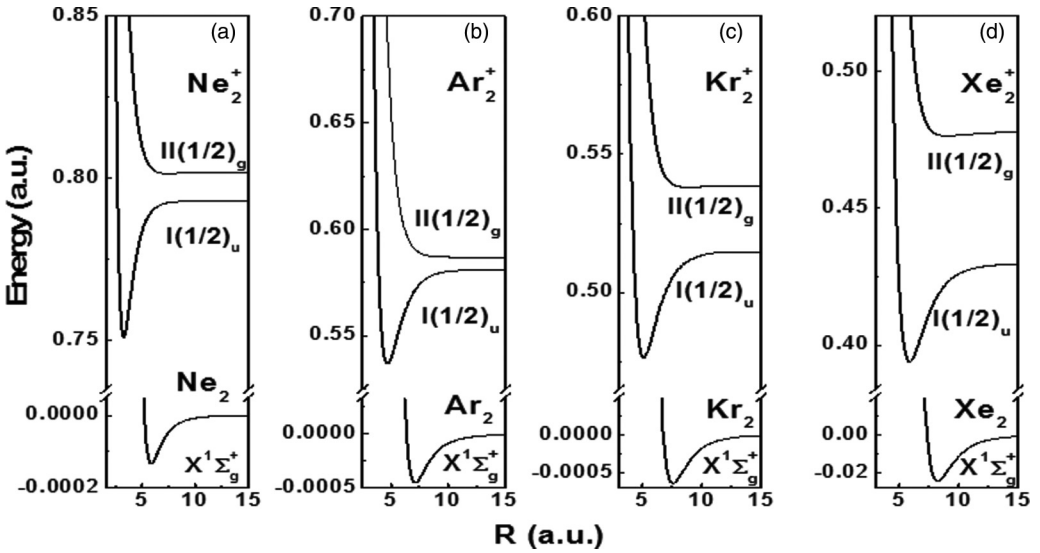

FIG. 3. Adiabatic potential energy curves for X_2 and X_2^+ dimers, calculated including spin-orbit coupling. (a) Ground state of Ne_2 (adapted from [20]) and the two lowest states of Ne_2^+ (from [21]). (b) Ground state of Ar_2 (from [22]) and the two lowest states of Ar_2^+ (from [23]). (c) Ground state of Kr_2 (from [25]) and the two lowest states of Kr_2^+ (from [26]). (d) Ground state of Xe_2 (from [25]) and the two lowest states of Xe_2^+ (from [27]).

with V_1 and V_2. Including the two lowest states of the X_2^+ dimer, we write the TDSE for this ionization-triggered process as

$$i\frac{d}{dt}\begin{pmatrix}\Psi_{\rm gr}\\ \Psi_1\\ \Psi_2\end{pmatrix} = \begin{pmatrix}V_{\rm gr}-i\Gamma_{\rm ADK} & 0 & 0\\ 0 & T_R+V_1+i\Gamma_{\rm ADK} & D_{21}\\ 0 & D_{12} & T_R+V_2\end{pmatrix}\begin{pmatrix}\Psi_{\rm gr}\\ \Psi_1\\ \Psi_2\end{pmatrix}. \quad (5)$$

$\Psi_{\rm gr}$ is a ground-state vibrational wave function obtained by imaginary time propagation in the ground state $V_{\rm gr}$ of X_2. $D_{ij}=E(t)d_{ij}$, $d_{ij}=\langle\Psi_i|R|\Psi_j\rangle$ are transition dipole matrix elements between two cation adiabatic electronic states. The combined external electric field $E(t)$ of the pump and probe pulse is

$$E(t,\tau)=E_{01}\cos[\omega_1(t)]\exp\left[-2\ln 2\left(\frac{t}{L_1}\right)^2\right] + E_{02}\cos[\omega_2(t-\tau)]\exp\left[-2\ln 2\left(\frac{t-\tau}{L_2}\right)^2\right]. \quad (6)$$

The pump (probe) pulse is assumed to have a Gaussian envelope with electric field amplitude E_{01} (E_{02}), frequency ω_1 (ω_2), and pulse length L_1 (L_2). The pulse lengths correspond to the full temporal width at half maximum of the pulse intensities.

After the probe pulse has passed, the wave packet is allowed to freely propagate for a sufficiently long time (500 fs). This allows the nuclear wave packet to completely enter the region $R > R_1$ where its bound part becomes separable from its dissociating part. We find the distance $R_1 = 10$ adequate to separate the bound from the dissociating nuclear motion and designate the dissociating part of the nuclear wave functions as $\Psi_i^{\rm diss}$ (Fig. 4) [34]. In order to determine the KER spectrum of the molecular ion, we Fourier transform the dissociating parts of the nuclear wave packet over the interval $[R_1,R_{\rm max}]$ to obtain the momentum representations

$$\tilde{\Psi}_i^{\rm diss}(P,t)=\int_{R_1}^{R_{\rm max}} dR\,\Psi_i^{\rm diss}(R,t)e^{-iPR}. \quad (7)$$

The distribution of the X^+ fragment energies as a function of the delay can then be written as

$$C^{\rm diss}(E,\tau)\propto\sum_i\left|\tilde{\Psi}_i^{\rm diss}(P,\tau)\right|^2, \quad (8)$$

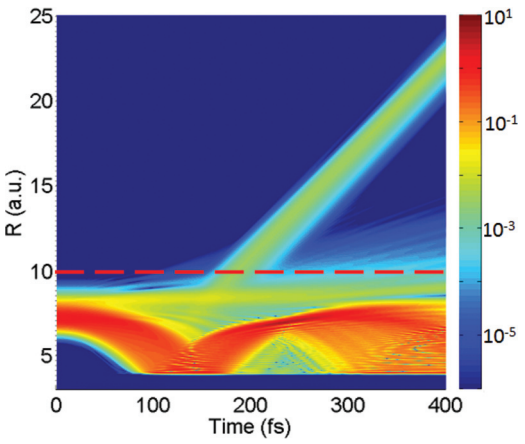

FIG. 4. (Color online) Probability density of the nuclear wave packet in the $^2\Sigma_u^+$ state of Ar_2^+ for a pump-probe delay of 150 fs and laser intensity of 10^{14} W/cm^2, calculated 500 fs after the end (FWHM) of the probe pulse. The pump and probe pulses have wavelengths of 800 and 1400 nm, respectively. The dashed red line corresponds to the assumed limit $R_1 = 10$ of the bound nuclear motion.

where $E = P^2/(2M)$ is the energy release and P is the final momentum per fragment. The total KER is twice E.

III. RESULTS AND DISCUSSION

A. Single-cation-curve calculations

We first discuss our numerical results for single-cation-curve calculations for the nuclear motion in X_2^+ dimers on $I(1/2)_u$ potential curves, i.e., including SO coupling [7,8,31]. The probability density (4) of the freely propagated vibrational wave packet in the $I(1/2)_u$ state of Ne_2^+, Ar_2^+, Kr_2^+, and Xe_2^+ is shown in Fig. 5. Our single-cation-curve calculations for the $^2\Sigma_u^+$ states (without SO couplings) yield similar probability densities with slightly different oscillation periods and full revival times (not shown). The full revival time and wave-packet oscillation periods for the wave-packet motion in the $^2\Sigma_u^+$ and $I(1/2)_u$ states, excluding and including SO coupling, respectively, are summarized in Table II. This table also lists

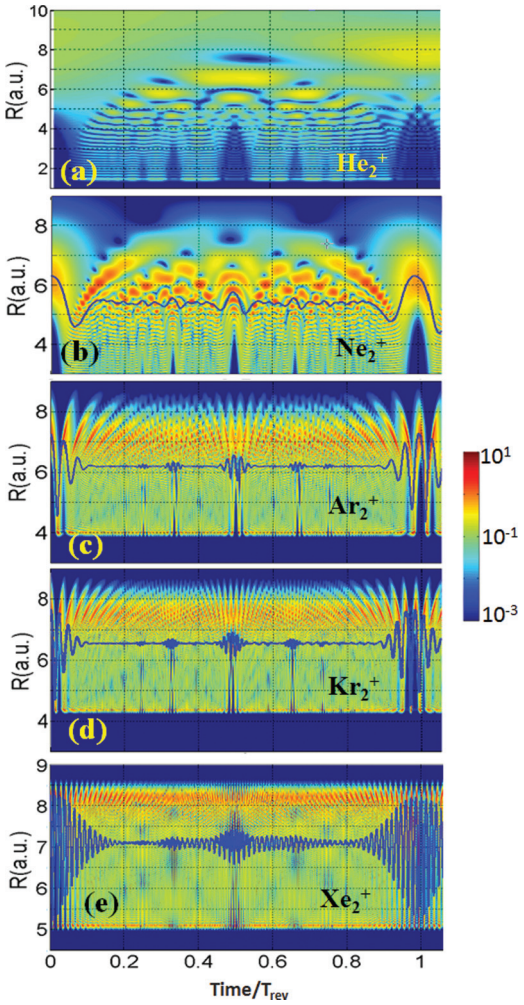

FIG. 5. (Color online) Probability density of X_2^+ nuclear wave packets as a function of the internuclear distance R for field-free propagation in the X_2^+ [$I(1/2)_u$] state (including spin-orbit coupling). (a) He_2^+, (b) Ne_2^+, (c) Ar_2^+, (d) Kr_2^+, and (e) Xe_2^+ dimers. The propagation time is given in units of the respective revival times. The X_2^+ wave packets are launched by an 800 nm, 80 fs, 10^{14} W/cm^2 laser pulse.

the number of bound vibrational states in both electronic cation states. The oscillation period and revival time for the Ar_2^+ $I(1/2)_u$ state are close to those observed [14].

The single-cation-curve calculations for the He_2^+ dimer show some periodic oscillatory structure and a revival time of the order of 525 fs, but do not allow the extraction of a vibrational oscillation period due to the very delocalized vibrational ground state of He_2 [Fig. 5(a)]. Table I summarizes some of the characteristic parameters of the noble-gas dimers and their cations, such as the SO splitting, reduced mass ($M/2$), ionization and dissociation energies, ground-state equilibrium distances, and the width of the ground-state probability densities as obtained from our calculations.

B. Classical versus quantum-mechanical characteristics of the nuclear vibrational motion

The number of oscillations during which the vibrational motion in the dimer cation dephases increases with the mass of the dimer [Figs. 5(b)–5(e)]. The nuclear wave packet dephases much slower for the Xe_2^+ dimer than for Ne_2^+. The number of vibrational oscillations the wave packet completes before dephasing is 1 for Ne_2^+, ∼3 for Ar_2^+, ∼ 5 for Kr_2^+, and ∼14 for Xe_2^+, indicating that heavier dimers more closely resemble classical particles, in compliance with the correspondence principle. In addition, the vibrational ground states of heavier dimers are more localized. For example, the ground-state probability density has a width of 0.5 a.u. for Xe_2 and ∼15 a.u. for He_2.

In order to quantify the "classical" character of the nuclear motion in X_2^+ cations, Fig. 6 compiles the calculated position and momentum variances $\Delta R^2 = \langle R^2\rangle - \langle R\rangle^2$ and $\Delta P^2 = \langle P^2\rangle - \langle P\rangle^2$, respectively, and the uncertainty product $\Delta R \Delta P$ for the $I(1/2)_u$ state as a function of time in units of the respective revival times. As shown in this figure and in the last colomn of Table II, the position variance in the $I(1/2)_u$ state can be more than one order of magnitude less for Xe_2^+ than for Ne_2^+, indicating significantly slower spreading of the nuclear wave packet in Xe_2^+. For this comparison in Table II, we calculated ΔR^2 after a propagation time of one vibrational oscillation period T_{osc} past the center of the pump pulse. The position variance oscillations are consistent with the wave-packet oscillations in the $I(1/2)_u$ states (cf. Fig. 5) and have pronounced minima at the revival times (corresponding to $t/T_{rev} = 1$ in Fig. 6). As the mass of the dimer increases, the minima become more distinctive. The same increase in classical character of the nuclear motion with increasing dimer mass is seen in the momentum variance and uncertainty product (middle and right column of Fig. 6, respectively).

C. Dipole-coupled calculations

The distinctive delay gap observed in KER spectra for Ar_2^+, with 800 and 1400 nm pump and probe pulses of 80 fs pulse length and 10^{14} W/cm^2 peak intensity is reproduced in our model calculations that include the dipole-coupled $I(1/2)_u$ and $II(1/2)_g$ states of the dimer cation [14]. It is of interest to see whether this particular feature of the delay-dependent Ar_2^+ KER spectrum is also present for other noble-gas dimers and

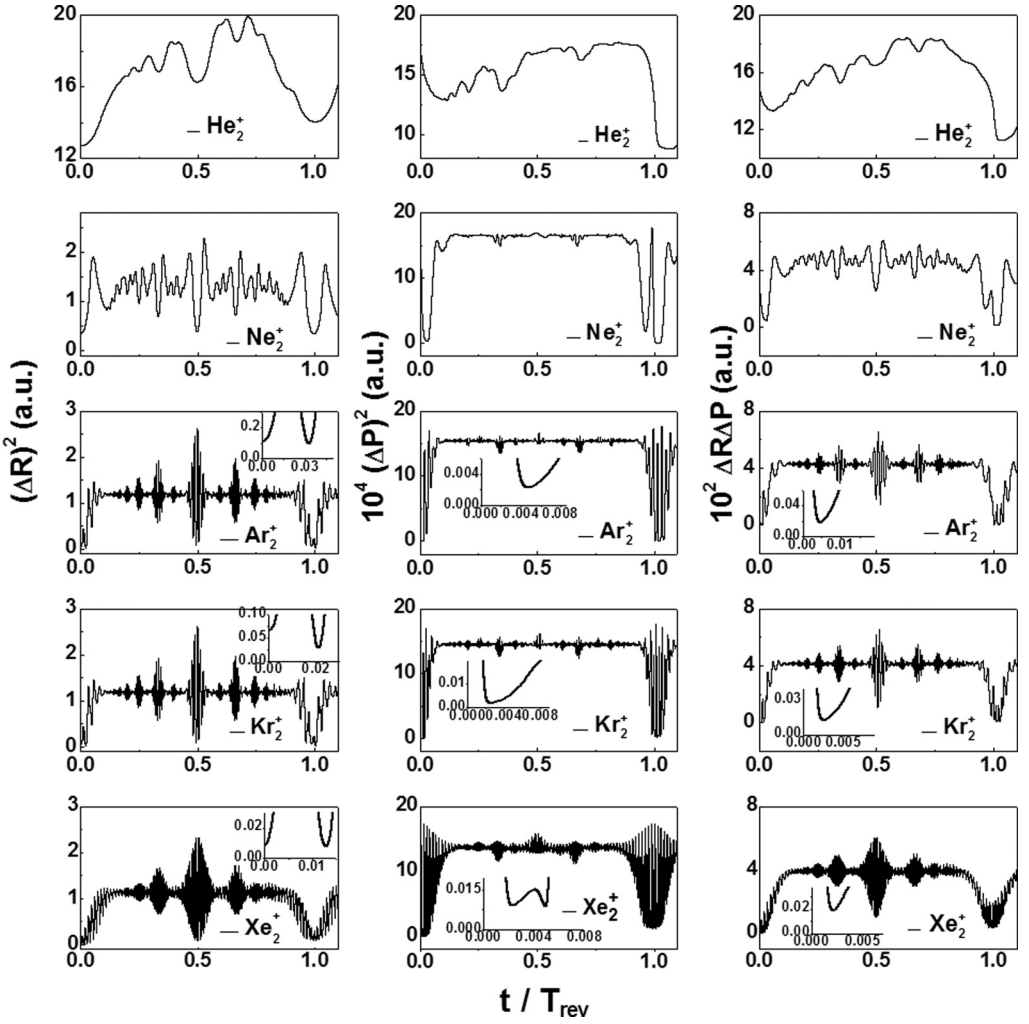

FIG. 6. Position variance $(\Delta R)^2$, momentum variance $(\Delta P)^2$, and uncertainty product $\Delta R \Delta P$ as functions of time scaled with the respective revival times for Ne_2^+, Ar_2^+, Kr_2^+, and Xe_2^+ noble-gas dimer cations in the $I(1/2)_u$ state. Due to the absence of a clear wave-function revival in our He_2^+ propagation calculation (for the $^2\Sigma_u^+$ state), we scale the time in the first row by the approximate revival time 525 fs. The insets zoom into small time intervals where the variances and the uncertainty product are minimal.

whether it has the same explanation. In this section we discuss calculations for X_2^+ molecular cations based on adiabatic potential curves that either disregard or include SO coupling. The term "energy band" used in the discussion below refers to the classically calculated expected KERs for one-photon dissociation and photon energies ω_1 and ω_2 (Table III). The classical estimates for the KER are obtained by approximating the nuclear dynamics as the motion of a point particle of reduced mass $(M/2)$ on a given adiabatic potential curve of the dimer cations [9].

KER spectra as a function of internuclear distance and pump-probe delay for calculations that include the dipole coupling in the pump and probe pulses of the states X_2^+ $(^2\Sigma_u^+)$ and X_2^+ $(^2\Sigma_g^+)$ are shown in Fig. 7. The parameters for the pump (probe) pulse used are 800 (1400) nm wavelength, 80 fs pulse length, and a peak intensity of 10^{14} W/cm^2, as in the experiment with Ar_2 [14]. The oscillating structures visible for the energy bands on both the negative (1400 nm pump) and positive (800 nm pump) delay side correspond to wave-packet

TABLE III. Expected KERs for calculations based on adiabatic molecular potential curves that include or do not include spin-orbit coupling. Calculations without spin-orbit coupling include the dipole-coupled $^2\Sigma_u$ and $^2\Pi_g^+$ states of the dimer cation; calculations with spin-orbit coupling include the $I(1/2)_u$ and $II(1/2)_g$ states.

	$^2\Sigma_u^+$		$I(1/2)_u$	
Dimer	KERs (eV) (800 nm)	KERs (eV) (1400 nm)	KERs (eV) (800 nm)	KERs (eV) (1400 nm)
He_2^+	1.6	0.8	1.6	0.8
Ne_2^+	1.45	0.75	1.3	0.6
Ar_2^+	1.35	0.6	1.18	0.45
Kr_2^+	1.3	0.54	0.24	0.008
Xe_2^+	1.2	0.5	0.1	
			KERs (500 nm)	KERs (700 nm)
Kr_2^+			1.0	0.4
Xe_2^+			0.9	0.26

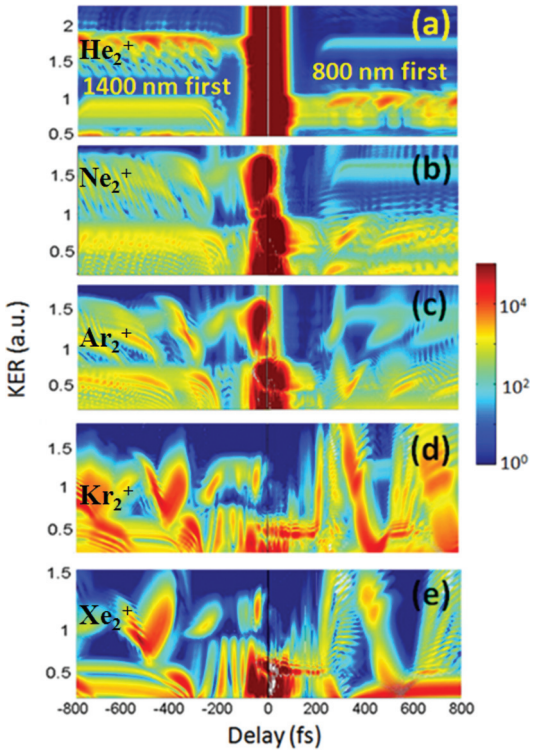

FIG. 7. (Color online) KER spectra as functions of the pump-probe delay for the dissociation of (a) He_2^+, (b) Ne_2^+, (c) Ar_2^+, (d) Kr_2^+, and (e) Xe_2^+. The calculations are based on dipole-coupled $^2\Sigma_u^+$ and $^2\Sigma_g^+$ states of the dimer cations that do not include spin-orbit coupling for 80 fs, 10^{14} W/cm^2 pump and probe pulses with wavelengths of 800 and 1400 nm.

oscillations in the $^2\Sigma_u^+$ states of X_2^+ with vibrational periods of ∼250 fs for Ne_2^+, ∼290 fs for Ar_2^+, ∼490 fs for Kr_2^+, and ∼550 fs for Xe_2^+ (Table II). The KER spectra reveal two separate energy bands that correspond to dissociation paths with two distinct avoided one-photon crossings for the 800 and 1400 nm pulses (see also Fig. 1). The delay gap in the upper energy band discussed in [14] occurs for positive delays only and extends over a delay range of the order of ∼150 fs in the KER spectra of He_2^+, Ne_2^+, and Ar_2^+ [Figs. 7(a)–7(c)].

Starting at negative delays, the main features of the KER spectra in Fig. 7 have the following interpretation. The 1400 nm pump pulse promotes part of the vibrational wave packet from the $^2\Sigma_u^+$ state to the $^2\Sigma_g^+$ state corresponding to a transition from point B to point E in Fig. 1. Subsequent dissociation by part of the nuclear wave packet along the upper molecular potential curve of the cation (labeled as V_2 in Fig. 1) yields the lower energy band in the KER spectra with energy releases in the 0.1–1.0 eV range. The remainder of the wave packet continues moving inward in the $^2\Sigma_u^+$ state until the 800 nm probe pulse couples it to the $^2\Sigma_g^+$ state (transition from point C to point D in Fig. 1), resulting in the upper energy band in the KER spectra with energy releases in the 1.0–1.9 eV range. For positive delays the pump-probe sequence is reversed. The 800 nm pulse pumps the wave packet from the ground state of X_2 to excited X_2^+ states. Subsequently, the 1400 nm probe pulse couples part of the wave packet into the excited X_2^+ ($^2\Sigma_g^+$) state (transition from point B to point E in Fig. 1), leading to the lower energy bands

TABLE IV. Results of the classically calculated propagation times from point A to point B and point B to point C in Fig. 1 along adiabatic potential curves of noble-gas dimer cations in their $^2\Sigma_u^+$ and $I(1/2)_u$ electronic states for the wavelength combinations 800 + 1400 and 500 + 700 nm.

	$^2\Sigma_u^+$ (800 + 1400 nm)		$I(1/2)_u$ (800 + 1400 nm)		$I(1/2)_u$ (500 + 700 nm)	
Dimer	t_{AB} (fs)	t_{BC} (fs)	t_{AB} (fs)	t_{BC} (fs)	t_{AB} (fs)	t_{BC} (fs)
Ne_2^+	22	9	21	12		
Ar_2^+	30	15	38	20		
Kr_2^+	36	29	0	46	51	28
Xe_2^+	45	42	0		50	53

in the KER spectra in Fig. 7. Subsequently, part of the wave packet is coupled from the lower X_2^+ ($^2\Sigma_u^+$) to the higher X_2^+ ($^2\Sigma_g^+$) state by the 800 nm pump pulse (transition from point C to point D in Fig. 1). In general, this one-photon coupling to point D in Fig. 1 results in dissociation with KERs in the higher energy band. However, the 1400 nm probe pulse may couple the wave packet back down to the $^2\Sigma_u^+$ state (transition from point E to point B in Fig. 1), leading to the delay gap in the KER spectra. This happens for He_2^+, Ne_2^+, Ar_2^+, and Kr_2^+ for pump-probe delays between ∼50 and 200 fs when the nuclear wave packet is near the 1400 nm avoided crossing (point E in Fig. 1) while the probe pulse is present [Figs. 7(a)–7(d)]. If the 1400 nm probe pulse arrives after the dissociating wave packet has passed this 1400 nm avoided crossing, down-conversion is no longer possible, and KERs within the higher energy band again occur. For Xe_2^+ the classical time (87 fs) the cation needs to expand its internuclear distance from point A to point C on the $^2\Sigma_u^+$ potential curve in Fig. 1, is larger than the pulse length (80 fs), explaining the absence of a continuous, delay-independent upper KER band for positive delays in Fig. 7(e) (Table IV).

Figure 8 summarizes our dipole-coupled calculations with the $I(1/2)_u$ and $II(1/2)_g$ states of the cations, including SO coupling. We used the same pulse parameters as in the calculations shown in Fig. 7. The delay gap is reproduced in these calculations for He_2^+, Ne_2^+, and Ar_2^+ [Figs. 8(a)–8(c)]. The KER spectra for Kr_2^+ and Xe_2^+ calculated for the 800 + 1400 nm wavelength combination [Figs. 8(d) and 8(e)] are dominated by KERs below 0.2 eV. The upper KER band is absent for Kr_2^+ and Xe_2^+ because the large SO splitting exceeds the photon energy and thus does not allow for an avoided crossing at 1400 nm wavelength to be overcome in a one-photon transition. For Kr_2^+ the photon energy at 1400 nm barely bridges the SO splitting, leading, instead to KERs close to zero (Table III). According to the expected KERs in Table III, the energy bands in the KER spectra in Figs. 7(b)–7(e) appear at lower energies compared to the spectra in Figs. 8(b)–8(e) (Table III). This lowering of the KER bands is most pronounced for the heavier dimers. It is an expression of fine-structure effects, as the width and depth of the $I(1/2)_u$ and the slope of $II(1/2)_g$ potential curves differ from the $^2\Sigma_u^+$ and $^2\Sigma_g^+$ potential curves due to SO coupling (cf. Figs. 2 and 3).

For Kr_2^+ and Xe_2^+ we have repeated our calculations for 500 + 700 nm pump-probe-wavelength combinations that

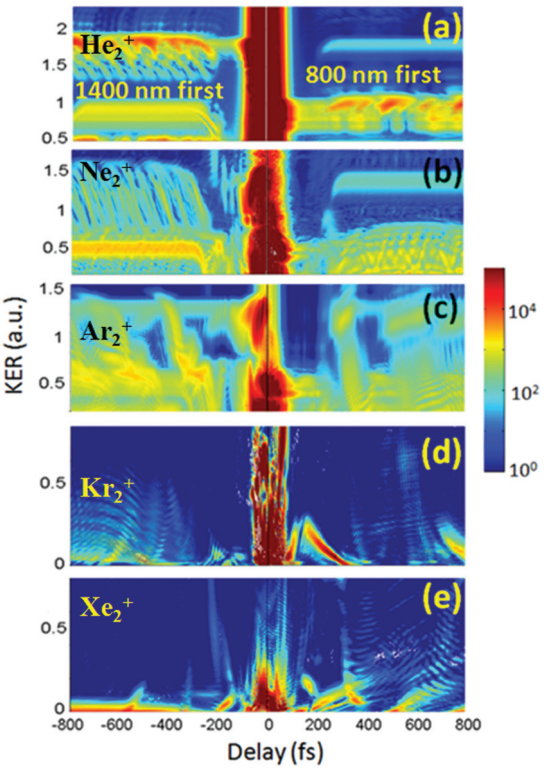

FIG. 8. (Color online) (a) Same as Fig. 7(a). (b)–(e) Same as Figs. 7(b)–7(e) but for dipole-coupled $I(1/2)_u$ and $II(1/2)_g$ states that include spin-orbit coupling.

allow for both lower and upper KER bands (Fig. 9). For this wavelength combination the double-banded energy structure at positive delays is not visible for the same reason as for the calculations excluding SO coupling in Fig. 7. For the shorter wavelength combination, the delay gap is present. We tentatively interpret it as we did for the lighter dimer cations [cf. Figs. 7(a)–7(c) and 8(a)–8(c)]. For Kr_2^+, the classically estimated time (79 fs) the wave-packet center needs to reach point C in Fig. 1 is about equal to the pulse length (80 fs). This travel time, however, is barely short enough for the wave packet to reach point C during the pump pulse. This may be seen as weak evidence for the delay gap at positive delays in Kr_2^+ being due to the same mechanism that operates in the lighter dimer cations. For Xe_2^+ the pulse length is shorter than the time (103 fs) the wave packet needs to transit from point A to point C (Fig. 1, Table IV). At the time the wave packet reaches point C (i.e., the 500 nm crossing), the pump pulse is gone, explaining

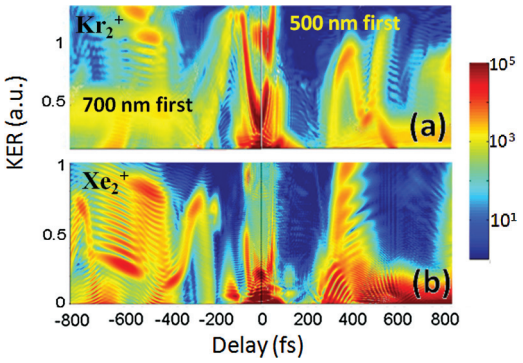

FIG. 9. (Color online) KER spectra as a function of the pump-probe delay for dipole-coupled $I(1/2)_u$ and $II(1/2)_g$ states of Kr_2^+ and Xe_2^+ including spin-orbit coupling. Parameters as in Figs. 8(d) and 8(e), but for 500 and 700 nm pump and probe pulses.

the absence of a KER band near 0.9 eV. Instead, the KER in Fig. 9(b) appears to simply portray wave-packet oscillations with a period of ∼530 fs.

IV. SUMMARY

We have investigated the dissociation dynamics in noble-gas dimers in two laser pulses of different wavelengths. The delay gap on the positive delay side in the KER spectra, observed previously for the Ar_2^+ dimer, is also present for He_2^+ and Ne_2^+ dimers. This striking feature can be explained within a wave-packet propagation model that describes the motion of vibrational cation nuclear packets on two adiabatic potential curves that become dipole coupled in the laser pulses. For Kr_2^+ and Xe_2^+ dimers the observed delay gap is tentatively explained with the same mechanism. Our study of the variances and uncertainty products reveals increasing classical characteristics of the nuclear wave-packet motion for increasingly massive dimers. In addition, we found that fine-structure effects become noticeable and eventually crucial (for Kr_2^+ and Xe_2^+) in KER spectra as the mass of the dimer increases.

ACKNOWLEDGMENTS

We thank R. Dörner and J. Wu for valuable discussions. This work was supported by National Science Foundation Grant No. PHY 1068752 and the Division of Chemical Sciences, Office of Basic Energy Sciences, Office of Science, US Department of Energy.

[1] J. Ullrich, A. Rudenko, and R. Moshammer, Annu. Rev. Phys. Chem. **63**, 635 (2012).
[2] C. Calvert, W. Bryan, W. Newell, and I. Williams, Phys. Rep. **491**, 1 (2010).
[3] Th. Ergler, A. Rudenko, B. Feuerstein, K. Zrost, C. D. Schröter, R. Moshammer, and J. Ullrich, Phys. Rev. Lett. **95**, 093001 (2005).
[4] A. S. Alnaser, B. Ulrich, X. M. Tong, I. V. Litvinyuk, C. M. Maharjan, P. Ranitovic, T. Osipov, R. Ali, S. Ghimire, Z. Chang, C. D. Lin, and C. L. Cocke, Phys. Rev. A **72**, 030702(R) (2005).
[5] B. Feuerstein, Th. Ergler, A. Rudenko, K. Zrost, C. D. Schröter, R. Moshammer, J. Ullrich, T. Niederhausen, and U. Thumm, Phys. Rev. Lett. **99**, 153002 (2007).
[6] M. Winter, R. Schmidt, and U. Thumm, Phys. Rev. A **80**, 031401 (2009).
[7] S. De, I. A. Bocharova, M. Magrakvelidze, D. Ray, W. Cao, B. Bergues, U. Thumm, M. F. Kling, I. V. Litvinyuk, and C. L. Cocke, Phys. Rev. A **82**, 013408 (2010); S. De, M. Magrakvelidze, I. A. Bocharova, D. Ray, W. Cao, I. Znakovskaya, H. Li, Z. Wang, G. Laurent, U. Thumm,

M. F. Kling, I. V. Litvinyuk, I. Ben-Itzhak, and C. L. Cocke, *ibid.* **84**, 043410 (2011).
[8] M. Magrakvelidze, C. M. Aikens, and U. Thumm, Phys. Rev. A **86**, 023402 (2012).
[9] I. A. Bocharova, A. S. Alnaser, U. Thumm, T. Niederhausen, D. Ray, C. L. Cocke, and I. V. Litvinyuk, Phys. Rev. A **83**, 013417 (2011).
[10] Y. H. Jiang, T. Pfeifer, A. Rudenko, O. Herrwerth, L. Foucar, M. Kurka, K. U. Kühnel, M. Lezius, M. F. Kling, X. Liu, K. Ueda, S. Düsterer, R. Treusch, C. D. Schröter, R. Moshammer, and J. Ullrich, Phys. Rev. A **82**, 041403(R) (2010).
[11] M. Magrakvelidze, O. Herrwerth, Y. H. Jiang, A. Rudenko, M. Kurka, L. Foucar, K. U. Kühnel, M. Kübel, Nora G. Johnson, C. D. Schröter, S. Düsterer, R. Treusch, M. Lezius, I. Ben-Itzhak, R. Moshammer, J. Ullrich, M. F. Kling, and U. Thumm, Phys. Rev. A **86**, 013415 (2012).
[12] L. Poisson, K. D. Raffael, M. Gaveau, B. Soep, J. Mestdagh, J. Caillat, R. Taïeb, and A. Maquet, Phys. Rev. Lett. **99**, 103401 (2007).
[13] W. Vassen, C. Cohen-Tannoudji, M. Leduc, D. Boiron, C. I. Westbrook, A. Truscott, K. Baldwin, G. Birkl, P. Cancio, and M. Trippenbach, Rev. Mod. Phys. **84**, 175 (2012).
[14] J. Wu, M. Magrakvelidze, A. Vredenborg, L. Ph. H. Schmidt, T. Jahnke, A. Czasch, R. Dörner, and U. Thumm, Phys. Rev. Lett. **110**, 033005 (2013).
[15] R. W. Robinett, Phys. Rep. **392**, 1 (2004).
[16] T. Niederhausen and U. Thumm, Phys. Rev. A **77**, 013407 (2008).
[17] T. Havermeier, T. Jahnke, K. Kreidi, R. Wallauer, S. Voss, M. Schöffler, S. Schössler, L. Foucar, N. Neumann, J. Titze, H. Sann, M. Kühnel, J. Voigtsberger, J. H. Morilla, W. Schöllkopf, H. Schmidt-Böcking, R. E. Grisenti, and R. Dörner, Phys. Rev. Lett. **104**, 133401 (2010).
[18] R. J. Gdanitz, J. Chem. Phys. **113**, 5145 (2000).
[19] F. X. Gadea and I. Paidarová, Chem. Phys. **209**, 281 (1996).
[20] A. Wüest and F. Merkt, J. Chem. Phys. **118**, 8807 (2003).
[21] J. S. Cohen and B. Schneider, J. Chem. Phys. **61**, 3230 (1974).
[22] Z. Ansari, M. Böttcher, B. Manschwetus, H. Rottke, W. Sandner, A. Veroef, M. Lezius, G. G. Paulus, A. Saenz, and D. B. Milošević, New J. Phys. **10**, 093027 (2008).
[23] T.-K. Ha, P. Rupper, A. Wüest, and F. Merkt, Mol. Phys. **101**, 827 (2003).
[24] W. J. Stevens, M. Gardner, A. Karo, and P. Julienne, J. Chem. Phys. **67**, 2860 (1977).
[25] P. Slavıček, R. Kaulus, P. Paška, I. Odvárková, P. Hobza, and A. Malijevský, J. Chem. Phys. **119**, 2102 (2003).
[26] R. Kalus, I. Paidarová, D. Hrivňák, P. Paška, and F. X. Gadéa, Chem. Phys. **294**, 141 (2003).
[27] I. Paidarová and F. X. Gadea, Chem. Phys. **274**, 1 (2001).
[28] W. R. Wadt, J. Chem. Phys. **73**, 3915 (1980); **68**, 402 (1978).
[29] See http://webbook.nist.gov/chemistry/.
[30] B. H. Bransden and C. J. Joachain, *Physics of Atoms and Molecules*, 2nd ed. (Prentice-Hall, New York, 2003); W. Demtröder, *Atoms Molecules and Photons* (Springer-Verlag, Berlin, Heidelberg, 2006).
[31] U. Thumm, T. Niederhausen, and B. Feuerstein, Phys. Rev. A **77**, 063401 (2008).
[32] M. Magrakvelidze, F. He, T. Niederhausen, I. V. Litvinyuk, and U. Thumm, Phys. Rev. A **79**, 033410 (2009).
[33] J. P. Brichta, W.-K. Liu, A. A. Zaidi, A. Trottier, and J. H. Sanderson, J. Phys. B **39**, 3769 (2006).
[34] F. He and U. Thumm, Phys. Rev. A **81**, 053413 (2010).